Characterization of the residual stresses in spray-formed steels using neutron diffraction

T.L. Lee,[a] J. Mi,[a,*] S.L. Zhao,[b] J.F. Fan,[b] S.Y. Zhang,[c] S. Kabra[c] and P.S. Grant[d]

[a]School of Engineering, University of Hull, Cottingham Road, Hull HU6 7RX, UK
[b]The Advanced Institute, Baosteel Co. Ltd., Shanghai, People's Republic of China
[c]ISIS Neutron Source, Science and Technology Facilities Council, Rutherford Appleton Laboratory, Didcot OX11 0QX, UK
[d]Department of Materials, University of Oxford, Parks Road, Oxford OX1 3PH, UK

Neutron diffraction was used to characterize the residual stresses in an as-sprayed tube-shaped steel preform. The measured residual stress distributions were compared with those simulated using finite element method by taking into account the effects of the thermal history, porosity and different phases of the sprayed preform. The porosity was measured using X-ray microcomputed tomography. The study revealed for the first time the correlation between the distribution of porosity and residual stress developed in the as-sprayed preform.

Porosity is common in spray-formed materials [1], especially at the base and top surface regions of the as-sprayed preforms (up to ~20%) [2], and is detrimental to the mechanical properties [3]. Hot isostatic pressing is often required to remove the porosity before the preform can be further processed or used directly. Porosity has also been shown by finite element (FE) modelling to affect the residual stresses in sprayed materials, especially when a critical porosity threshold is exceeded [4]. The bonding integrity between the particles in the preform and at the preform–substrate interface plays a critical role in determining the material's mechanical properties and performance, while the residual stresses associated with the preform cooling can also become a primary cause of premature failure [5]. Recently, Ristau et al. [6] used FE modelling to study the development of residual stresses in sprayed preforms by taking into account the thermal history during the spray forming and subsequent heat treatment, but stresses were not validated experimentally. Direct measurement of stress development during spray forming is generally not feasible due to the harsh environment and experimental complexity. However, the residual stress can be characterized non-destructively after spraying using diffraction techniques. Ho and Lavernia [7] used laboratory-based X-ray diffraction but, due to the micrometre penetration depth of the X-rays, measurements were confined to the near-surface region [8], which is generally subjected to substantial stress relaxation. Neutron diffraction (ND) offers more capability since neutrons can penetrate most metallic materials up to a few centimetres [9]. The recent development of third-generation neutron strain scanners offers the prospect of at least an order of magnitude improvement in counting times [9], and such scanners have been successfully used to characterize the residual stress in "thick" engineering materials [10]. Until now, there has been no ND characterization of the residual stresses in spray-formed components and how to account for and interpret the link between the as-sprayed porosity and the residual stresses.

In this paper, X-ray microcomputed tomography (μCT) was used to quantify the porosity distribution of an as-sprayed steel preform and ND was used to characterize the residual stress distribution through the preform thickness with varying porosity. The relationship between porosity and residual stresses was studied and interpreted by FE modelling.

An as-sprayed tube-shaped preform was manufactured by Baosteel (China). ASP30 steel was sprayed onto a pre-heated T91 steel tube substrate (773 K and 66 rpm rotation) using a closed-coupled gas atomizer with nitrogen gas at a pressure of 1.3 MPa. The melt pouring temperature was 1843 K and the average melt flow rate was 0.5 kg s^{-1}. The preform was sprayed with multiple passes under the metal spray for 170 s using a substrate horizontal travel velocity of 5 mm s^{-1}. A 10 mm wide and 20 mm thick ring of the spray-formed steel was sectioned from one end of the preform for residual stress measurements. Microstructural

---

* Corresponding author. Tel.: +44 1482 465670; e-mail: j.mi@hull.ac.uk

characterization revealed that interfacial bonding was not achieved between the substrate and the preform, and that the preform had two distinct layers (Fig. 1a): a high-density inner layer and a lower-density (porous) outer layer. The dense layer was formed in the first few passes with droplets from the initial hot spray, while the more porous layer developed in subsequent passes under a progressively colder spray because of the reducing melt hydrostatic pressure in the tundish and thus reducing melt flow rate. Samples ($2 \times 2 \times 20$ mm) were cut from the ring and the through-thickness porosity distribution was measured using an X-ray μCT scanner (HMX 160; X-Tek Systems) with a voxel size of $5.93 \times 5.93 \times 5.93$ μm^3. AVIZO v.6.3.1 software was used to segment the 3-D data set.

Residual strains in the ring were measured in the radial (ε_r), hoop (ε_θ) and axial (ε_z) directions using the time-of-flight (TOF) neutron diffractometer at ENGIN-X, ISIS Neutron Source [9]. The sample and ND set-up are shown in Figure 1a. The scan step size was 1 mm and a gauge volume (GV) of $1 \times 4 \times 4$ mm (1 mm in the ε_r direction) was used for ε_θ and ε_z, while $4 \times 4 \times 4$ mm was defined for ε_r. Due to the ε_r scan orientation, the larger GV was necessary to maintain a symmetrical GV shape. It is well documented that a partially filled GV can shift the neutron-weighted centre of gravity (ncog) from the GV geometric centre of gravity (gcog), resulting in artificial peak shifts and pseudo-strains [11]. The GV in the experiment was meticulously positioned in the sample using theodolites to ensure complete filling and any near surface (partially filled GV) measurements were disregarded. Along the scanned path, the effect of porosity distribution in the GV on the shift in the ncog (Fig. 1c) was determined by calculating the centre of mass of the material in the GV and the corresponding pseudo-strains generated due to the ncog shift were determined relative to the detector at $2\theta = 90°$ using [11]:

$$\varepsilon_{P_s} = \frac{\Delta L}{L} + \cot\frac{2\theta}{2} \cdot \frac{\Delta 2\theta}{2} \qquad (1)$$

where 2θ and L are the diffraction angle and neutron flight path length from the gcog to the detector, respectively, and $\Delta 2\theta$ and ΔL are their corresponding changes due to the ncog shift. Figure 1b shows that the maximum ncog shift occurred when the GV was in the steep porosity gradient region, with no ncog shift in regions without porosity gradients. The slight ncog shift at the dense region (4–6 mm from interface) was because the GV contained some porosity in the GV vertex region (GV diagonal of 5.66 mm). The calculated maximum compressive pseudo-strain was ~35 μɛ (Fig. 1b) which is about one-fifth of the average ND measurements uncertainty (~170 μɛ). Pseudo-strains due to vertical ncog shifts are much smaller than those due to lateral shifts [11], so were ignored. Hence, it was assumed that the error caused by the pseudo-strains due to porosity did not affect the final stress distribution significantly.

Whole-pattern Rietveld refinements via GSAS [12] were used to obtain the lattice parameters d and phase weight fractions (PWFs) from the TOF diffractograms. The residual strain was calculated using $\varepsilon = (d–d_0)/d_0$, where d_0 is the stress-free lattice parameter. Coupons of dimensions $5 \times 20 \times 30$ mm (20 mm in the ε_r direction) were sectioned from the ring using electrical discharge machining. Annealing heat treatment (1173 K, furnace cooled at 10 K h^{-1} to 973 K, then freely to ambient temperature) was applied to two coupons to obtain stress-free samples for d_0 measurement. However, the heat treatment resulted in the
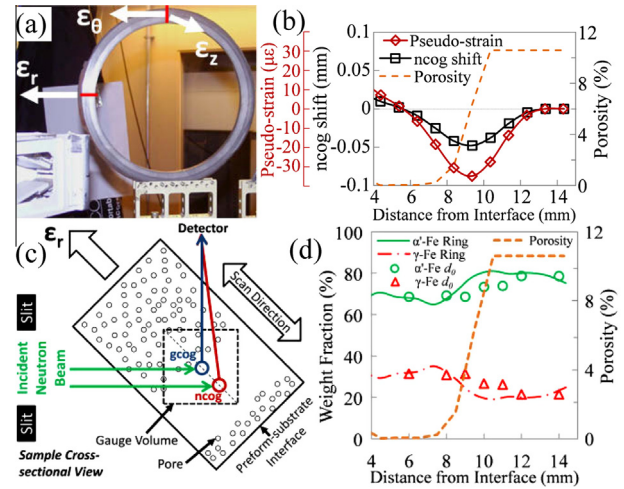
Figure 1. (a) The ND experimental set-up at ENGIN-X showing the etched ring sample, (b) the calculated ncog shift and the corresponding pseudo-strains, (c) a schematic diagram of the neutron beam path scattered from the gcog and ncog and (d) ring and stress-free sample PWF distributions.

decomposition of metastable austenite (γ-Fe) and the as-sprayed phase fractions were no longer representative. Therefore, the as-sprayed coupon was used as the d_0 sample. Figure 1d shows the PWF distributions for the ring and the d_0 coupon, measured using the same scan configuration, indicating the same distributions of martensite (α'-Fe) and γ-Fe in both samples. The measured d_0 values from the coupon were averaged for each phase and used as the d_0 for subsequent estimates of principal residual strains.

The residual strains measured are macrostrains since the GV (= 64 mm^3) was much larger than the length scale of the microstructure or the porosity in the material (typically 10^{-3}–10^{-2} mm^3). Under a condition of elastic deformation, any localized variations in the principal stress direction caused by the free surfaces of the randomly distributed and oriented porosity should be averaged out at this macrolength scale. The arrangement is qualitatively similar to variations of principal strains in non-porous materials with micrometre grains in the form of intergranular stresses, which are assumed to average out in the measurements from a large GV [8]. The corresponding residual stresses, σ_i can be calculated from the measured strains using Hooke's law:

$$\sigma_i = \frac{E}{1+v}\left[\varepsilon_i + \frac{v}{1-2v}(\varepsilon_r + \varepsilon_\theta + \varepsilon_z)\right] \qquad (2)$$

where subscript i denotes the respective principal stresses, E is the Young's modulus and $v = 0.3$ is the Poisson's ratio. The TOF diffractograms (Fig. 2a) showed that α'-Fe and γ-Fe were the dominant phases, as reported in similar as-sprayed steel alloys [13]. The bulk residual stress, $\sigma_{\alpha'+\gamma}$ can be determined from the phase-specific residual stress using a rule of mixture (ROM) [14]:

$$\sigma_{\alpha'+\gamma} = f_{\alpha'}\sigma_{\alpha'} + (1 - f_{\alpha'})\sigma_\gamma \qquad (3)$$

where $f_{\alpha'}$ is the α'-Fe PWF, $\sigma_{\alpha'}$ and σ_γ and are the α'-Fe and γ-Fe phase stress, respectively, which were calculated using Eq. (2), with the Young's modulus of each phase estimated from the corresponding steel, i.e. 200 GPa for α'-Fe and 193 GPa for γ-Fe [15]. Figure 2b shows the residual
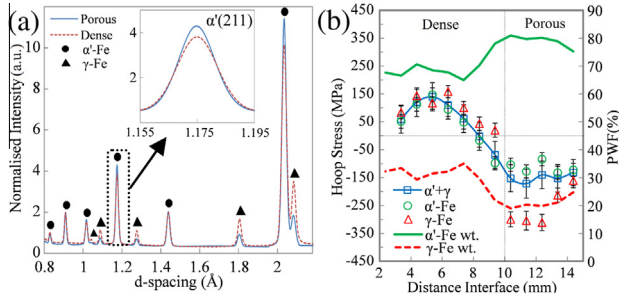
Figure 2. (a) The superimposed TOF diffractograms scanned from the dense and porous regions of the preform and (b) the PWF distribution across the preform thickness, and the bulk and phase residual hoop stress distributions.

hoop stress calculated for the bulk and each phase based on their PWF.

In general, thermal residual stresses are developed when mismatch in strain arises due to coefficient of thermal expansion (CTE) variations between the constituent materials in the preform [7] and differences in thermal history between the deposited layers. The PWF distribution has a lower weight fraction of γ-Fe in the porous region due to the increased metal droplet cooling rate of the colder, reduced-flow rate spray, which causes more γ-Fe to transform into α'-Fe. The CTE (up to 922 K) of α'-Fe is 11.6 μK^{-1} and that of γ-Fe is 18.7 μK^{-1} [15], and the bulk CTE (α'-Fe + γ-Fe) can be calculated using a ROM similar to Eq. (3). A simple 3-D FE model based on COMSOL Multiphysics® was derived from the model in Refs. [16,17] and was used to simulate the thermal history and thermal stress in the preform. For simplicity, each deposition layer was modelled as a 1 mm thick ring (10 mm wide) and the tube-shaped preform was modelled by adding 20 such layers. The thermophysical properties of the sprayed steel were taken from Ref. [15] and the boundary conditions for heat transfer were from Refs. [2,17]. At the preform top surface, convective heat transfer coefficients of 650 and 35 $W\,m^{-2}\,K^{-1}$ were assumed during and after spraying, respectively, and there was radiative heat transfer with an emissivity of 0.5. The preform–substrate interface was defined with an interfacial heat transfer coefficient of 1000 $W\,m^{-2}\,K^{-1}$ [2]. The impinging droplet temperature, T_d, was determined using:

$$T_d = (1 - f_L)T_S + f_L T_L \qquad (4)$$

where f_L is the liquid fraction of the droplets (0.65 for the dense and 0.4 for the porous region), and T_S and T_L are the solidus and liquidus temperature of steel, respectively. The assumed values of f_L in Eq. (4) were estimated from empirical relationship between the droplet liquid fraction and the porosity of the spray-formed tube preforms [18]. The simulated temperature distribution immediately after spraying is shown in Figure 3b. The thermal strains for the deposit layers were calculated using:

$$\varepsilon_{th} = \alpha(T - T_{sf}) \qquad (5)$$

where α is the material CTE tensor, T is the final temperature of the sprayed layer and $T_{sf} = 1158$ K is the stress-free temperature above which most steels, including high-strength steels [19], lose their strength. The residual stress, σ, in the FE model was calculated using:
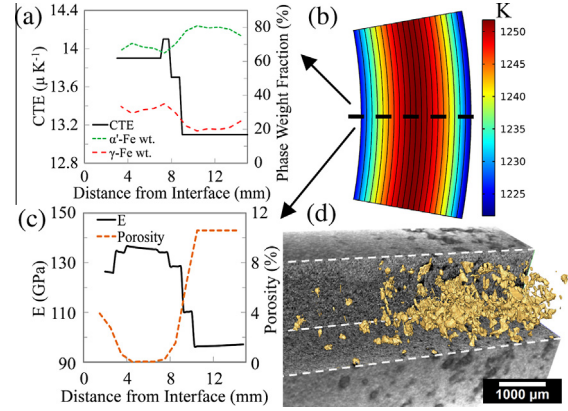
Figure 3. (a) Mean CTE (up to 922 K) distributions due to PWF variation, (b) temperature distribution in the preform simulated using the FE model (20° sector cross-section) just after the spray ended, (c) Young's modulus distribution due to porosity and (d) a cutaway view of the X-ray μCT 3-D rendering of the porosity at the dense-to-porous transition region.

$$\sigma = C : (\varepsilon - \varepsilon_{th}) \qquad (6)$$

where C is the fourth-order elasticity tensor and ε is the total strain tensor. An isotropic and linear elastic material model was used, and solidification and phase transformation effects were not considered. The effect of porosity on the temperature-dependent material properties was incorporated by specifying each deposit layer with local values of E and ν, which were calculated using the models reported in Refs. [20–22]:

$$E_{Porous} = E_D \left[\frac{(1 - P)^2}{1 + (2 - 3\nu)P} \right] \qquad (7)$$

where $E_D = 240$ GPa for the dense steel [15] and P is the fraction of porosity. ν for each deposit layer was determined using [21]:

$$\nu_{Porous} = (\nu + 1)\left(\frac{0.41 - P}{0.41} \right)^{0.0855} - 1 \qquad (8)$$

Figure 3d shows a typical cutaway view of the 3-D rendering of the porosity at the dense-to-porous transition region. The mean CTE and E distributions due to the variation in PWF and porosity across the preform thickness are shown in Figure 3a and c, respectively.

At the dense-to-porous transition region, the two adjacent deposit layers with different CTEs and initial temperatures (colder towards the end of the spray process) constrain each other during cooling and the thermal strain mismatch can be expressed as:

$$\varepsilon_{mismatch} = \alpha_1 \Delta T_1 - \alpha_2 \Delta T_2 \qquad (9)$$

In order to take into account the effect of the colder deposition conditions on the stress development, the boundary at the dense-to-porous transition region of the FE model was constrained to the equilibrium point of extension or contraction between the two layers during cooling. A similar constraint was defined at the preform–substrate interface to take into account the constraining effect of the substrate. With the aforementioned procedure, the model indirectly considers the change in spray conditions, taking into account the effects of porosity
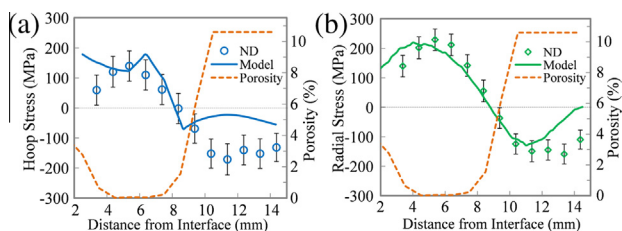
Figure 4. (a) Hoop and (b) radial residual stress distributions in the as-sprayed preform from ND measurements and FE modelling with μCT porosity measurements.

distribution on the material properties and the CTE variation between each layer to quantify the residual stresses generated, and was compared with the ND measurements. The residual stress in the axial direction was not the focus in this study since it would be relaxed when the ring sample was cut from the preform.

Figure 4a shows that, within the necessary simplifications of the model, the calculated hoop stress distribution generally agreed well with the ND measurements. The difference increases towards the preform–substrate interface because adhesion across the interface was not perfect and some stress relaxation was expected, especially where any debonding might occur. Along the preform thickness, a tensile stress of ~150 MPa was developed in the denser regions, while compressive stresses of ~150–200 MPa were present in the porous region. The steep stress gradient from +150 MPa to −200 MPa shown at the dense-to-porous transition region was due to the large difference in CTE between the dense and porous regions, and this change was also apparent from the TOF diffractograms (Fig. 2a), where the $\alpha'(211)$ peak from the dense region was shifted to the right, indicating a more tensile residual strain in that region. Radial stress distributions (Fig. 4b) showed a similar profile and, again, a transition, with a slightly higher tensile stress (220 MPa) in the dense region. The lower stress measured towards the interface region was again likely due to stress relaxation caused by some limited debonding. Higher compressive stresses in the porous region were generally caused by any steeper temperature gradients between the adjacent deposit layers due to the intermittent multi-passes of the spraying with reducing liquid fraction, which is well known to promote porosity. Nevertheless, within the confines of the simplifying assumptions, the model predicted the general trend of the stress distributions well.

In summary, residual stress distributions in an as-sprayed steel preform were characterized using neutron diffraction and showed tensile residual stresses up to 220 MPa in dense regions and compressive stresses of up to 200 MPa in more porous regions, as the deposition conditions changed. There was a steep stress gradient in the dense-to-porous transition region. The residual stress distributions predicted by the FE model agreed relatively well with neutron diffraction measurement results, and highlighted the inter-dependence of local thermal history, phase fraction and porosity on residual stress profile development in as-sprayed preforms.

[1] P.S. Grant, Prog. Mater. Sci. 39 (1995) 497–545.
[2] C. Cui, U. Fritsching, A. Schulz, Q. Li, Acta Mater. 53 (2005) 2775–2784.
[3] E.J. Lavernia, Y. Wu, Spray Atomization and Deposition, John Wiley, New York, 1996.
[4] E. Celik, O. Sarikaya, Mater. Sci. Eng., A 379 (2004) 11–16.
[5] R.T.R. McGrann, D.J. Greving, J.R. Shadley, E.F. Rybicki, T.L. Kruecke, B.E. Bodger, Surf. Coat. Technol. 108–109 (1998) 59–64.
[6] R. Ristau, A. Becker, V. Uhlenwinkel, R. Kienzler, Simulations of temperatures, residual stresses, and porosity measurements in spray formed super alloys tubes, in: Superalloy 718 and Derivatives, John Wiley & Sons, Inc., 2010, pp. 470–485.
[7] S. Ho, E.J. Lavernia, Scr. Mater. 34 (1996) 527–536.
[8] P.J. Withers, H.K.D.H. Bhadeshia, Mater. Sci. Technol. 17 (2001) 355–365.
[9] J.R. Santisteban, M.R. Daymond, J.A. James, L. Edwards, J. Appl. Crystallogr. 39 (2006) 812–825.
[10] S.Y. Zhang, A. Evans, E. Eren, B. Chen, M. Pavier, Y. Wang, S. Pierret, R. Moat, B. Mori, Neutron News 24 (2013) 22–26.
[11] P.J. Withers, M.W. Johnson, J.S. Wright, Physica B 292 (2000) 273–285.
[12] A.C. Larson, R.B.V. Dreele, Los Alamos National Laboratory Report LAUR 86–748, 2004.
[13] F. Yan, Z. Xu, H. Shi, J. Fan, Mater. Charact. 59 (2008) 592–597.
[14] D. Yu, K. An, Y. Chen, X. Chen, Scr. Mater. 89 (2014) 45–48.
[15] Available from: <http://www.matweb.com/>.
[16] J. Mi, P.S. Grant, Acta Mater. 56 (2008) 1588–1596.
[17] J. Mi, P.S. Grant, Acta Mater. 56 (2008) 1597–1608.
[18] L. Warner, C. Cai, S. Annavarapu, R. Doherty, Powder Metall. 40 (1997) 121–125.
[19] J. Chen, B. Young, B. Uy, J. Struct. Eng. 132 (2006) 1948–1954.
[20] N. Chawla, X. Deng, Mater. Sci. Eng., A 390 (2005) 98–112.
[21] J. Kováčik, J. Mater. Sci. 41 (2006) 1247–1249.
[22] N. Ramakrishnan, V.S. Arunachalam, J. Am. Ceram. Soc. 76 (1993) 2745–2752.